



Effective periodate activation by peculiar Cu₂O nanocrystal for antibiotics degradation: The critical role of structure and underlying mechanism study

Yubiao Li^a, Jinpeng Wang^a, Zhenlun Wei^a, Wanqing Li^a, Wanqing Duan^a, Xuezhen Feng^b,
Qiang Ma^a, Qingwen Zhang^a, Hong Chen^{b,*}, Xiaoyong Wu^{a,*}

^a School of Resources and Environmental Engineering, Wuhan University of Technology, Wuhan 430070, China

^b School of Environmental Science and Engineering, Southern University of Science and Technology, Shenzhen 518055, China

ARTICLE INFO

Keywords:

Fenton-like reaction
Crystal edges
Cu₂O
Periodate
Wastewater

ABSTRACT

Exploring efficient catalyst and unveiling relevant intrinsic mechanism for pollutants control based on periodate (PI) activation is urgently required. Herein, an effective catalyst Cu₂O with peculiar exposed facets and crystal edges was firstly developed to activate PI towards antibiotic wastewater degradation. Intriguingly, Cu₂O nanocrystals with {100}+{111} co-exposed facets together with their shared crystal edges exhibited the intrinsic high catalytic activity, and 88.90% of tetracycline (20 mg L⁻¹) could be rapidly degraded within 5 min with $k_{obs} = 0.378 \text{ min}^{-1}$, which outperformed the {100}, {110}, {111} solely exposed ones or {100}+{110}, {100}+{110}+{111} co-exposed ones. A comprehensive mechanism study revealed that the crystal edges of {100}/{111} in Cu₂O nanocrystals are conducive to better electron transfer, charge separation, and PI adsorption properties, thus triggering highly efficient PI activation over other crystal edges exposed nanocrystals. Besides, {100}/{111} crystal edges in Cu₂O crystal made the PI activation-induced antibiotic degradation change from the non-radical/radical mixed reaction to ¹O₂ (75.71%) dominated nonradical reaction. This work provides systematical insights into constructing effective catalysts for wastewater treatment via structure engineering.

1. Introduction

With the development of medical industry, the antibiotics released in natural water have aroused ever-increasing attention owing to their long-term threat to the human bodies. Among multifarious antibiotics, tetracycline (TC) is widely used to treat diseases in humans, livestock and aquatic products [1]. The high structural stability and resistance of TC make it difficult to be completely degraded in natural environment [2]. Therefore, it is urgent to develop efficient and green TC wastewater treatment methods. Advanced oxidation processes (AOPs) have been considered as one of the most effective strategies for corresponding wastewater treatment due to their high efficiency of decontamination and relatively environmental-friendly [3,4]. Among various oxidants based AOPs (H₂O₂, peracetic acid, hypochlorous acid, etc.), periodate (IO₄⁻) based AOPs attracted peculiar attention for antibiotics wastewater treatment due to its higher selectivity and easier storage and transportation than other oxidants [5]. However, the development for high efficiency of activators for periodate is still limited as compared with other oxidants based AOPs and more efforts are urgently required.

Cu₂O as a star semiconductor material has been widely used in the fields of electrocatalysis, photocatalysis, conductivity and sensor, etc. because of its low cost, outstanding physical and chemical properties [6–9]. It also has been utilized as activators for AOPs, but rarely reports about Cu₂O activated periodate. Besides, the interfacial structure is a crucial factor that regulates the performances of the materials for sensors, electrocatalysis, photocatalysis, AOPs, etc. [10–12], owing to the discrepancy of the interfacial atom arrangement, surface energy, as well as electronic property [13]. Tremendous research has been devoted to studying structure-property relationships of the preferred orientated exposure facets in single crystalline nano-catalysts. The highly preferred crystal facets in a dedicated catalyst frequently provide precise surface chemistry dynamics, which is of great importance to the fundamental reaction mechanism elucidation [14–17]. Diverse surface structures and different surface chemistry may occur with the exposure facets varied on the exact composition nano-catalyst. In this regard, many literature reports have been dedicated to the facet engineering of single crystalline nanocrystals [15–18]. However, the crystal edges formed between different crystalline facets have been ignored for a long time [19]. As for

* Corresponding authors.

E-mail addresses: chenh3@sustech.edu.cn (H. Chen), parawu521@whut.edu.cn (X. Wu).

<https://doi.org/10.1016/j.apcatb.2023.123351>

Received 8 July 2023; Received in revised form 11 September 2023; Accepted 27 September 2023

Available online 29 September 2023

0926-3373/© 2023 Elsevier B.V. All rights reserved.

nano-sized crystals, the atoms on the crystal edges occupied a large ratio of all the exposed surface atoms. It is of great interest and emergence to consider the intrinsic catalytic reactivity of crystal edges for the single crystalline nano-sized heterogeneous catalysts. Therefore, Cu_2O should be a good activator candidate to construct excellent performance by crystal facet and edges engineering and further explore the aforementioned crystal edge effects in periodate based AOPs for wastewater treatment.

Herein, a library of seven kinds of Cu_2O nano-sized single crystals with solely {100}, {110}, {111} or multiple facets mixture from {100}, {110}, {111} exposure was synthesized. AOPs based on periodate (PI) activation under the assistance of simulated solar light (SSL) was employed as a model reaction to study the corresponding catalytic performances of Cu_2O with different facets/crystal edges. Interestingly, based on a comprehensive study, we find that the nanocrystals with multi-facets exposing to form {111}/{100} crystal edge are beneficial for periodate activation and result in highly efficient pollutants degradation. While the catalytic effects of {111}/{110} and {100}/{110} crystal edges are insignificant or even pose adverse effects. In addition, the performance of crystals with multi-facets of {111}/{100} crystal edge is closely related to the relative ratio of {111} to {100}. These observations have been well supported by comprehensive density functional theory (DFT) calculations, electrochemical tests, and in-situ microcalorimetry techniques. The present work provides deep insights into the critical crystal edge effects of single crystalline nanocrystals for regulating catalytic performance, which paves the way for developing highly efficient AOPs catalysts via edge engineering.

2. Materials and methods

2.1. Synthesis of Cu_2O nanocrystals with different facets

Synthesis of Cu_2O with {100}, {111}, and {100}+{111} facets. 10 mL NaOH (2 M) was added dropwise to 100 mL (10 mM) $\text{CuCl}_2 \cdot 2\text{H}_2\text{O}$ solution under a 55 °C water bath, and kept stirring for 0.5 h. Subsequently, 10 mL ascorbic acid (0.6 M) was added dropwise and aged for 3 h. Finally, the red brick precipitate was centrifuged and washed three times with ethanol and ultrapure water, and then dried in vacuum oven at 60 °C for 6 h to obtain cubic Cu_2O (100). The octahedral (111), truncated cubic (100 +111-1) and truncated octahedral (100 +111-2) Cu_2O nanocrystals were synthesized following a similar recipe referring to the cubic Cu_2O (100) nanocrystals. The difference was that $\text{CuCl}_2 \cdot 2\text{H}_2\text{O}$ solution was mixed with 6.2 g (for 111), 4 g (for 100 +111-1) and 6 g (for 100 +111-2) polyvinylpyrrolidone before dropwise adding NaOH.

Synthesis of Cu_2O with {110} facets. Rhombic dodecahedron Cu_2O (110) crystal was synthesized in a 34 °C water bath. With vigorous stirring, SDS (0.087 g) was added to the mixed solution containing 6.92 mL ultrapure water and 0.5 mL (0.1 M) $\text{CuCl}_2 \cdot \text{H}_2\text{O}$. After the SDS was dissolved, 0.18 mL (1 M) NaOH was added, and then 2.4 mL (0.1 M) $\text{H}_3\text{NO} \cdot \text{HCl}$ was injected within 5 s. The string was stopped after 20 s and kept in a 34 °C water bath for 1 h. Finally, the red brick precipitate was centrifuged at 5000 rpm, collected, washed twice with 6 mL ethanol/pure water of 1:1 vol ratio, and dried in a vacuum oven at 60 °C for 6 h to obtain the rhombic dodecahedron Cu_2O (110) nanocrystals.

Synthesis of Cu_2O with {100}+{110} and {100}+{110}+{111} facets. $\text{CuSO}_4 \cdot 5\text{H}_2\text{O}$ (2 mmol) and EDTA (1 mmol) were dissolved in 30 mL ultrapure water, then mixed solution was heated to 55 °C and kept for 30 min. Subsequently, 25 mL (1.6 M for 100 +110, 3.96 M for 100 +110 +111) NaOH was added dropwise. After 5 min, 0.5 g of hydroquinone was added and stirred for 1 h. Finally, the precipitate was collected by centrifugation at 8000 rpm, washed three times with ethanol and ultrapure water, and dried in vacuum oven at 60 °C for 6 h to obtain the edge-truncated cube Cu_2O (100 +110) or edge- and corner-truncated octahedra Cu_2O (100 +110 +111).

2.2. Catalytic activity evaluation

The catalytic activity of different facets Cu_2O for PI activation under SSL was evaluated with the TC degradation experiment. Typically, Cu_2O (10 mg) and TC solution (100 mL, 20 mg L^{-1}) were stirred in a quartz beaker for 30 min with circulating cooling water in the dark to reach adsorption-desorption equilibrium. Then, PI (0.5 mM) was added and the simulated sunlight (SSL, 300 W xenon-lamp with AM 1.5 filter glass) was turned on. At the specified time intervals (0, 0.5, 1, 2, 3, 4 and 5 min), the reaction liquid (3 mL) was withdrawn and quenched with $\text{Na}_2\text{S}_2\text{O}_3$ (0.1 mL, 1 M). The above liquid was centrifuged and the supernatant was taken to measure the residual TC concentration. In catalytic stability test, the reacted Cu_2O was collected, washed with ultrapure water, and dried before being used for the next pollutant degradation. In the first catalytic stability test, 12 sets of parallel degradation experiments were performed to obtain sufficient reacted Cu_2O for 5 stability tests.

In addition, detailed information about reagents, characterizations and analytical methods are presented in Text S1-S8.

3. Results and discussion

3.1. Characterizations of as-prepared Cu_2O

A library of single crystalline Cu_2O nanocrystals has been synthesized by tuning the surface energy with different surfactant dosages [20, 21]. First, XRD was used to determine the crystal structure of as-synthesized Cu_2O (Fig. S1). The XRD patterns of seven samples within the library suggest the as-synthesized Cu_2O are well crystallized in the crystallographic cubic phase Cu_2O (PDF#05-0667) free of impurities. Besides, the relative diffraction peak intensities summarized in Table S1 varied, implying that the single crystalline Cu_2O nanocrystals are crystallized in different preferentially exposed facets. For example, the {200}:{111} peak intensity ratio of the pure {100} facet-exposed sample is significantly higher than that of the pure {111} facet-exposed sample, indicating that {100} is the dominant exposed facet of the sample. Similarly, a relatively high {110}:{111} ratio indicates that {110} is the dominant facet in the sample. Fig. 1 presents the morphology structure of as-prepared seven Cu_2O nanocrystals. As shown in Fig. 1a–g, the obtained Cu_2O crystals are of fine-tuned homogenous morphologies. The corresponding exposed facets can be identified to be {100}, {110}, {111}, {100}+{110}, {100}+{111}-1, {100}+{111}-2, {100}+{110}+{111}, respectively, via electron crystallography approach (Figs. S2-S8) [22,23]. The particle sizes of the nanocrystals are around 500 nm (Figs. S9 and S10) with a similar specific surface area (Figs. S11 and S12). The schematic diagrams of the above seven single crystalline nanocrystals are illustrated in Fig. 1h–n. Distinct crystal edges of {100}/{100}, {110}/{110}, {111}/{111}, {100}/{110}, {110}/{111} and {100}/{111} are preserved in the seven as-synthesized nanocrystals as labeled with thick lines in the unfolded models. The corresponding crystal structure models of the crystal facets and edges are shown in Fig. 1o–t. Meanwhile, the relevant co-exposed facet ratio and crystal edges in Cu_2O crystals are summarized in Table S2. A series of characterizations collectively demonstrate that Cu_2O with different exposed facet and corresponding crystal edges has been successfully synthesized, which is suitable to unveil the effect of crystal edges on the periodate based AOPs performance.

3.2. Improved catalytic performance by crystal edges

The catalytic activity of Cu_2O is evaluated by the activation of PI under simulated solar light (SSL), and the representative antibiotic of tetracycline (TC) is selected as the target pollutant. It is worth noting that 88.9% of TC could be quickly degraded within 5 min in the Cu_2O -(100 +111-2)/PI/SSL system (Fig. 2a), which is significantly higher than the solo photo or Cu_2O mediated PI activation. To eliminate the

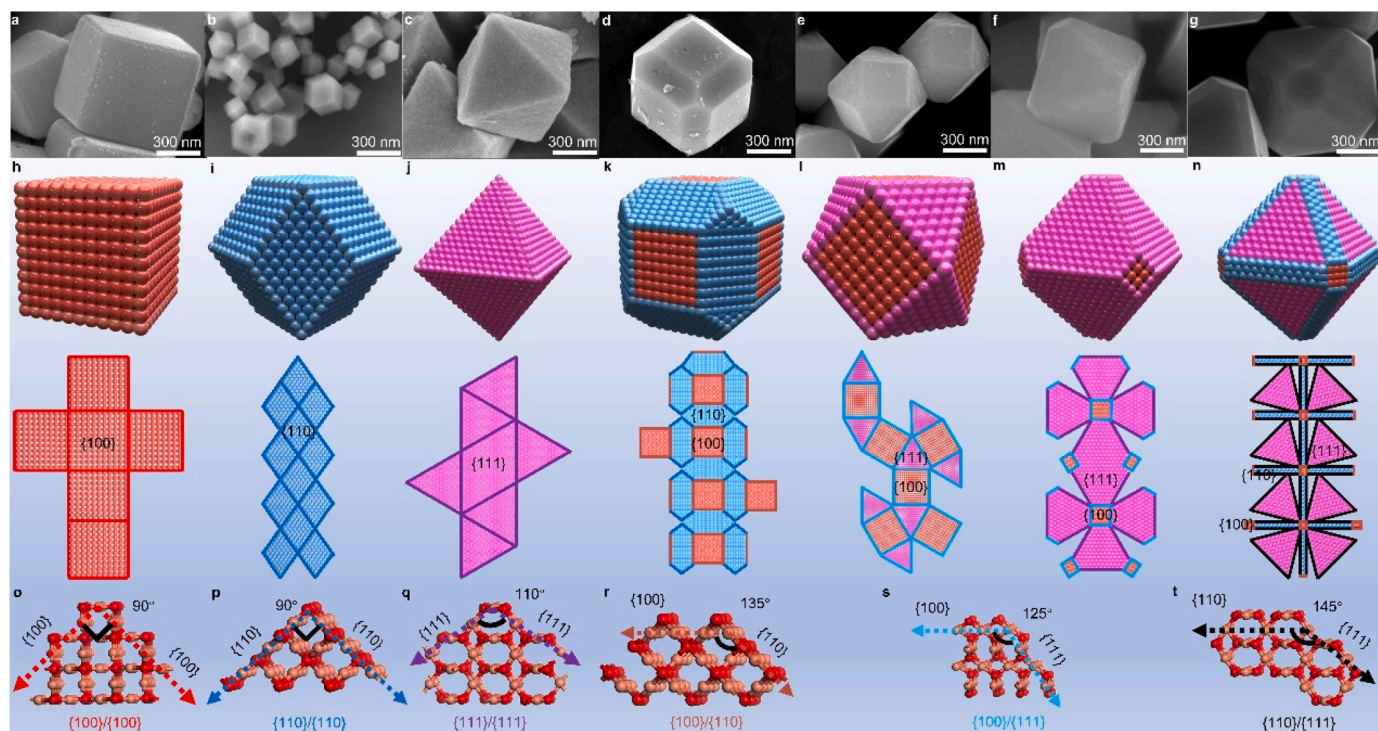


Fig. 1. Characterization of different morphology Cu₂O nanocrystals. (a–g) SEM images of Cu₂O crystals. (h–n) Schematic diagrams of Cu₂O with various exposed facets and crystal edges as well as corresponding unfolded models. (o–t) Crystal edges of the seven different nanocrystals.

influence of homogeneous catalysis, the contribution of leached Cu²⁺ on TC degradation was explored, and a minor removal efficiency similar to the PI/SSL system was achieved within 5 min (Fig. S13). This result indicates that the homogenous catalysis shows a negligible effect on TC degradation. Therefore, it is speculated that the Cu₂O crystal and SSL have a synergistic effect on PI activation. The degradation performance of Cu₂O with different exposed facets and shared crystal edges is compared in Fig. 2b, c. For the mono-facet exposure ones, Cu₂O with {111} facet exposure exhibited an 8% and 20% higher degradation efficiency than {100} and {110}, respectively. For the multi-facets co-exposure crystals, Cu₂O exposed {100}+{111} facets displayed a better catalytic performance than those of {100}+{110} and {100}+{110}+{111} co-exposed ones and even superior over that of pure {111} exposed one. The above phenomena indicate that there are different synergistic catalytic effects between different facets/crystal edges and SSL. Therefore, the performance of Cu₂O about the photocatalytic degradation of TC with different exposed facets/ crystal edges and that of PI activation in the absence of SSL are compared to clarify the synergistic effect (Figs. S14 and S15). All samples exhibited poor TC removal in Cu₂O/PI (< 35%) or Cu₂O/SSL (< 15%) system, further indicating the indispensability of both Cu₂O and SSL. Besides, since all samples have small specific surface areas (Figs. S11 and S12) and present the inconsistent trends of adsorption efficiency (Fig. S16) with that of catalytic performance, the possibility about that the different activities are caused by specific surface areas can be ruled out. So the above results solidly verified that the crystal facet and edge of Cu₂O significantly affect the PI activation induced TC degradation activity. Moreover, the corresponding pseudo first-order rate constants (k_{obs}) based on degradation rate of seven Cu₂O samples under various conditions are presented in Fig. 2d. The k_{obs} of Cu₂O under SSL are much higher than the superposition of individual systems (Cu₂O/PI or SSL/Cu₂O), especially the {100}+{111} facets, which means that the crystal edge formed by {100} and {111} facets have higher catalytic activity for PI activation under SSL.

To illustrate the in-depth correlations between the interfacial structure and catalytic activity, further experiments were conducted by

artificially mixing the pure facets exposed nanocrystals based on their relative facet ratios (Table S2 and Texts S5, S6) of multiple-facets co-exposed samples of {100}+{110}, {100}+{110}+{111}, {100}+{111}-1, {100}+{111}-2 (Fig. S17). Comparing the interface difference of the artificially mixed sample with the same mass and similar surface area of native multiple-facets co-exposed ones, it is obvious that the interfacial difference between pure {100}, {111} exposed nanocrystals and {100}+{111} co-exposed nanocrystal should be contributed by the crystal edges as displayed in Fig. 1h–n. To investigate the effects of crystal edges on PI activation, we compared the k_{obs} of four co-exposed facets samples with those artificially mixed ones. The theoretically calculated k_{obs} based on the relative ratios in co-exposed facets crystal are shown in Fig. 2e and the experimental part. Interestingly, {100}+{111}-2 co-exposed Cu₂O nanocrystals presented a k_{obs} value of 0.378 min⁻¹, which is higher than the artificially mixed and theoretically calculated ones of 0.322 min⁻¹ and 0.352 min⁻¹, respectively. Furthermore, compared with pure {100} and {111} nanocrystals, the Cu₂O {100}+{111}-1 sample with relatively long {100}/{111} crystal edges presented further improved (ca. 0.05 min⁻¹) k_{obs} value than that (ca. 0.024 min⁻¹) of the sample Cu₂O {100}+{111}-2 with relatively shorter {100}/{111} crystal edges, while for {100}+{110} and {100}+{110}+{111} co-exposed samples with {100}/{110} and {110}/{111} crystal edges, the k_{obs} value was adversely smaller than those of manually mixed and theoretical calculated pure ones.

The above results solidly confirm that the {100}/{111} crystal edge is positively correlated to the catalytic kinetics and plays a critical role in enhancing the catalytic performance, while the {100}/{110} and {110}/{111} edges contribute less distinct or even adverse effects. Moreover, the improved catalytic performance of {100}/{111} edges is closely related to the ratio of {100}/{111} crystal edges in the nanocrystals.

In addition, the activation performance of other Fenton-like oxidants such as peroxydisulfate (PDS), peroxymonosulfate (PMS) and H₂O₂ were explored to verify the universality of the crystal edge effect of Cu₂O nanocrystals (Fig. 2f and S18–S20). The tendency of k_{obs} value evolution remains similar as in PI-induced Fenton-like reaction towards TC

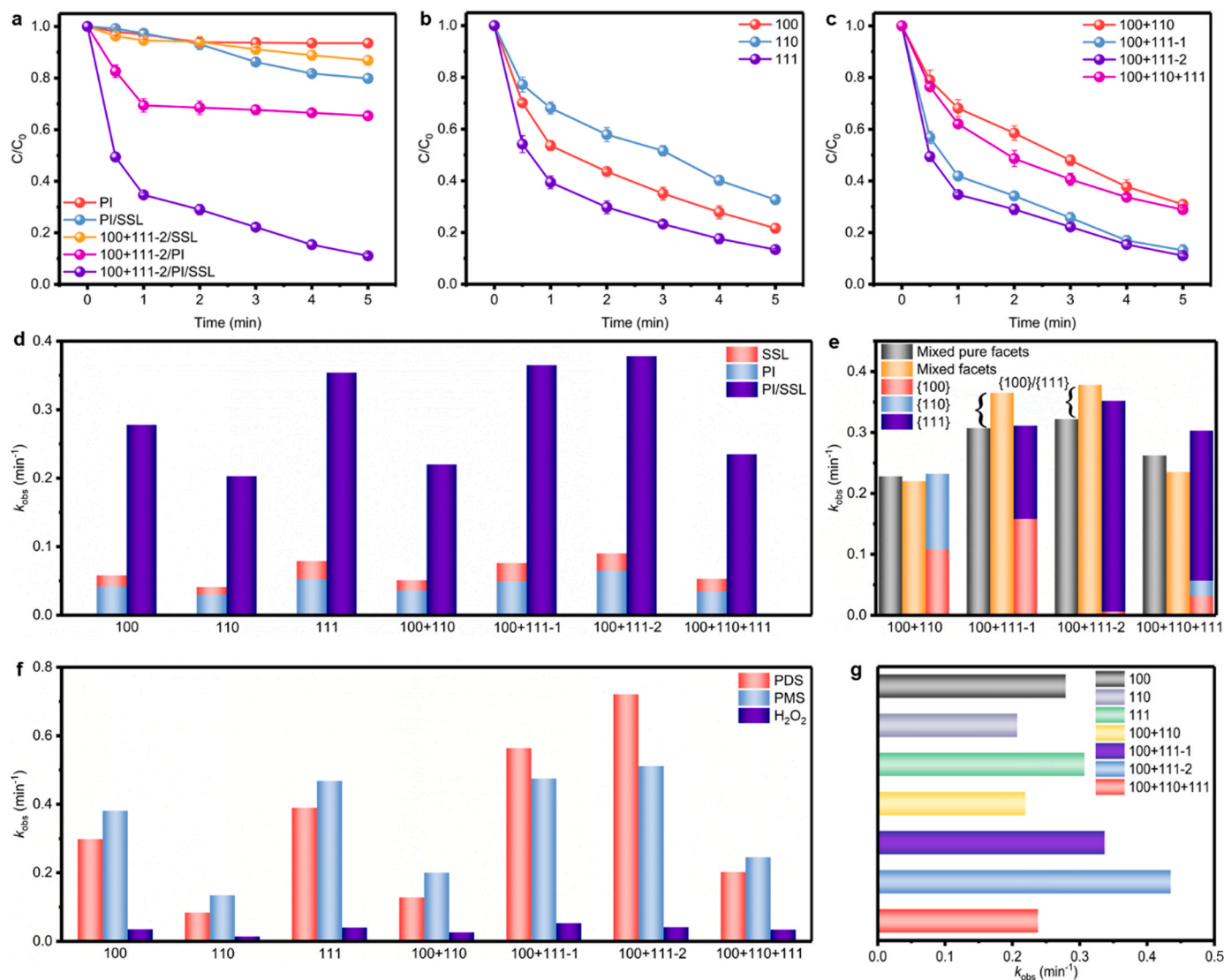


Fig. 2. Catalytic performance of different Cu₂O samples. (a–c) Time-dependent degradation activity. (d) k_{obs} under various catalytic conditions. (e) Comparison of k_{obs} values of Cu₂O single nanocrystals with multi-exposed facets and Cu₂O crystals with artificially mixed pure ones, as well as the theoretically calculated k_{obs} values. (f) k_{obs} of Cu₂O catalyzed TC degradation with different oxidants. (g) k_{obs} of Cu₂O catalyzed RhB degradation. ([TC]₀ = 20 mg L⁻¹, [RhB]₀ = 20 mg L⁻¹, [Cu₂O]₀ = 0.1 g/L, [oxidants]₀ = 0.5 mM).

degradation regardless of oxidant types. Furthermore, when TC has been replaced by the commonly-used dye RhB, the tendency can be well preserved (Fig. 2g and S21). Therefore, the crystal edge effect of Cu₂O can be extended to most of existing AOPs for the treatment of organic wastewater.

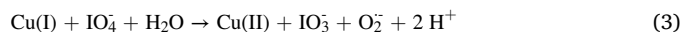
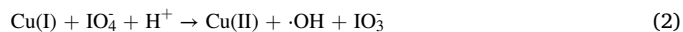
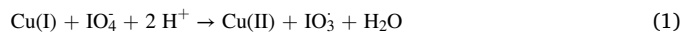
3.3. Catalytic mechanism of Cu₂O crystals

3.3.1. Reactive species identification

To unveil the degradation mechanism of TC under Cu₂O-activated PI aqueous solution, quenching experiments have been carried out, as shown in Fig. 3a and S22. It has been found that IO₃⁻, h⁺ and ·OH made minor or ignorable contributions for all samples. In contrast, O₂^{·-} and ¹O₂ played significant roles in TC degradation, especially over sample with {100} + {111}–2 exposed facets, which should be owing to the particularly exposed facet and as-formed {100}/{111} crystal edges.

The above results have been well evidenced by the EPR tests as shown in Fig. 3b, S23 and S24. As the signals of ·OH over {100} + {111} + 2 exposed samples declined significantly as compared to those of {100} and {110} exposed specimens, while for ¹O₂, the corresponding

signals were greatly enhanced, implying the dominant contributions of ¹O₂ in the system with {100}/{111} crystal edges. It can be concluded that the existence of {100}/{111} crystal edges in Cu₂O crystal made the PI activation-induced TC degradation change from the non-radical/radical mixed reaction to ¹O₂ dominated nonradical reaction. As for O₂^{·-} signals (Fig. S24), previous reports have proved that electron-rich organics are difficult to be degraded by anionic charged O₂^{·-}, so it is speculated that O₂^{·-} acts as a precursor of ¹O₂ [24]. Moreover, it has been confirmed from the atmosphere experiment and dissolved oxygen consumption (Figs. S25 and S26) that the O₂ reduction made a secondary contribution while the IO₄⁻ activation made a dominant contribution for the O₂^{·-} generation to ¹O₂. Referring to previously reported works [25–27], it can be proposed that the following reactions Eqs. (1–5) would happen in the Cu₂O-induced PI activation:



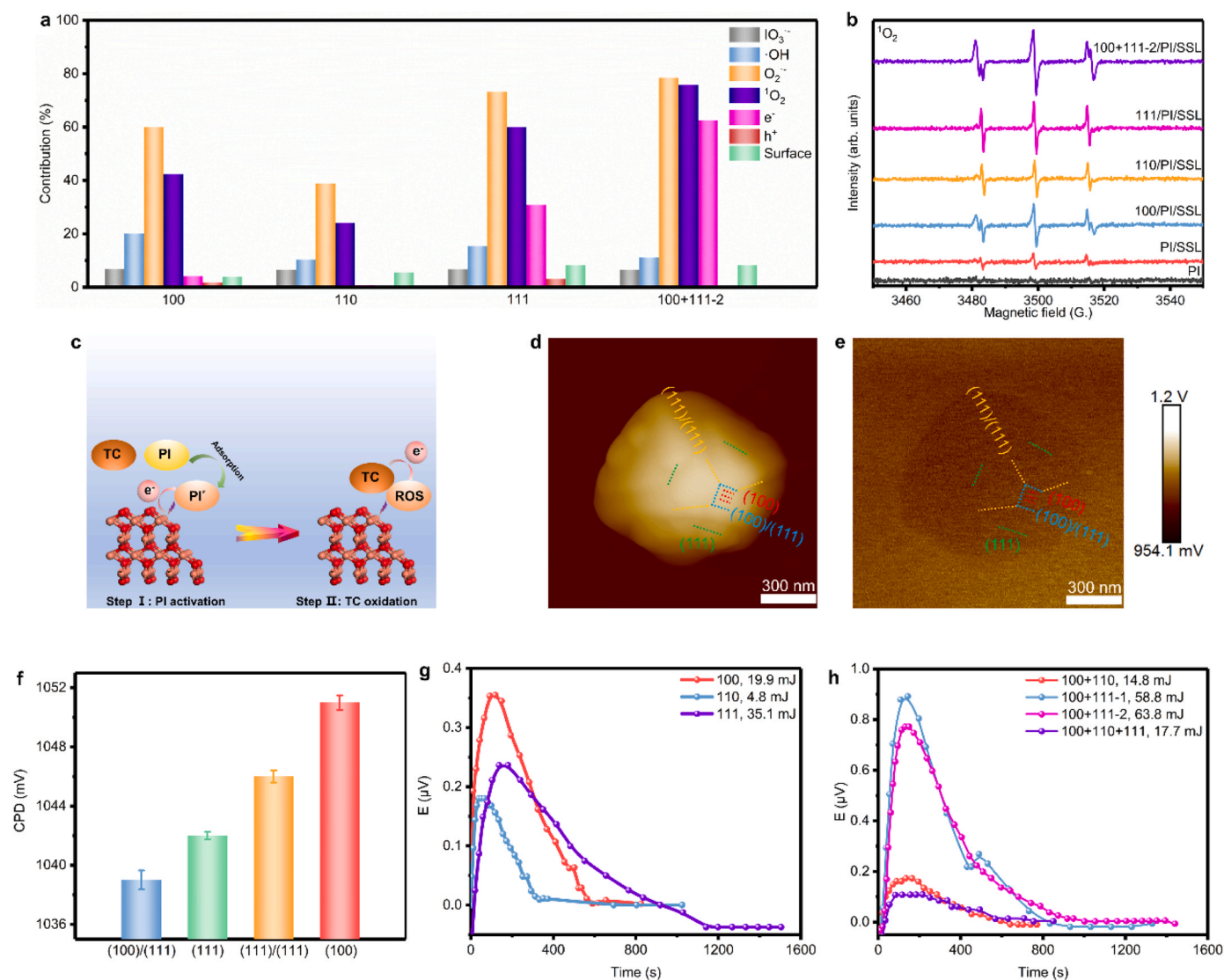
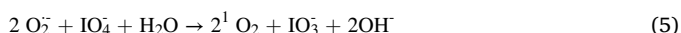


Fig. 3. Degradation mechanism of TC via Cu₂O catalyzed PI activation. (a) Trapping experiments. (b) EPR signals of ¹O₂. (c) TC degradation mechanism. (d–f) Topographic, corresponding CPD maps and values of Cu₂O crystal with {100}+{111}–2 co-exposed facets. (g, h) *In-situ* microcalorimetry spectra during Cu₂O activate PI process. ([TC]₀ = 20 mg L⁻¹, [Cu₂O]₀ = 0.1 g/L, [PI]₀ = 0.5 mM).



Besides, Fig. S27 plots the FTIR spectra of pristine and used Cu₂O samples. A new band locates at 779 cm⁻¹ appeared in the used sample, which is ascribed to the signal of Cu–I bond. It means that strong adsorption between Cu₂O with {100}/{111} crystal edge and IO₄⁻ occurred. Meanwhile, it verified previously that Cu₂O presented weak adsorption for TC pollutants (Fig. S16), and there is no relevant relationship between TC adsorption and *k*_{obs} value (Fig. S28). Therefore, the activation of PI mainly occurs on Cu₂O surface, while the degradation of TC mainly occurs in aqueous solution. The corresponding reaction mechanism of PI activation for TC degradation over Cu₂O could be deduced in Fig. 3c. 1) PI has been adsorbed on Cu₂O crystal surface and then was activated to produce the dominated ¹O₂ species; 2) Reactive species diffuse into the aqueous solution and attack the TC molecules. The overall degradation process is dominated by a heterogeneous reaction of Cu₂O interface for PI activation to generate reactive oxygen species, followed by a homogeneous reaction of active species with TC [28].

3.3.2. Electron transfer enhanced by crystal edges

From the discussion mentioned above, it can be concluded that the superior catalytic activity of Cu₂O with {100}+{111} co-exposed facets should be attributed to the favorable adsorption and effective electron transfer between Cu₂O and PI induced mainly by {100}/{111} crystal edge. To further clarify the mechanism of improved PI activation induced by {100}/{111} crystal edge, KPFM analysis, electrochemical measurement, *in-situ* microcalorimetry test and DFT calculations were carried. Fig. 3d–f shows the KPFM images of the Cu₂O sample with {100}+{111}–2 co-exposed facets. From the topographic and underlying contact potential difference (CPD) images, it could be found that a heterogeneous potential distribution has been preserved within the Cu₂O crystal surface. The {100}/{111} crystal edges with blue lines exhibited a lower CPD value (1039 mV) than those of {111}/{111} crystal edges (1046 mV), {100} (1051 mV) and {111} (1042 mV) facets, indicating that the {100}/{111} crystal edges in this crystal preserve a lowest local work function. In this case, {100}/{111} crystal edges are beneficial for electron transfer and photogenerated electron-hole separation, which are conducive to PI activation [29–31].

To further understand the electron conductivity, Nyquist plots have been collected, as shown in Fig. S29. The Cu₂O crystal with {100}+

{111}—2 exposed facet presents the smallest arc size in the Nyquist plot among all the seven samples [32–34]. Besides, the LSV and CV curves suggest that the {100}+{111} crystal edges are more reductive than the mono {100} or {111} facets (Figs. S30 and S31), which is beneficial for PI to receive electrons on the surface and be activated. More importantly, {100}+{111}—2 has the highest current value under light irradiation (Fig. S32), implying that its photogenerated electron-hole separation is superior to other facets/crystal edges and is beneficial for PI activation under light irradiation [32,33]. Whereas the two Cu₂O crystals with {100}+{110} and {100}+{110}+{111} exposed facets respectively exhibited relatively similar or even poorer charge transfer capability than those of pure {100}, {110} and {111} exposed ones. These electro/photochemical measurements confirmed that {100}/{111} crystal edges are effective for photoelectron production and electron transfer from Cu₂O to PI, while the {100}/{110} and {110}/{111} crystal edges played minor or negative roles.

Besides, to determine the energy variation in PI activation process of different Cu₂O samples, in-situ microcalorimetry test was carried [35]. As presented in Fig. 3g, h, the Cu₂O sample with {111} exposed facet exhibited about 35.1 mJ energy release in Cu₂O/PI system, which is much higher than those of {100} and {110} exposed facet. Moreover, the Cu₂O sample with {100}+{111}—2 co-exposed facets demonstrated the highest energy release of 63.8 mJ and a relatively long releasing time (1000 s) among seven crystals. However, the two Cu₂O samples with {100}+{110} and {100}+{110}+{111} co-exposed facets respectively displayed similar or much lower energy releases

compared with the corresponding solely exposed ones. When TC was added to Cu₂O/PI system, the energy release and reaction time were increased, meaning that the TC addition promoted the PI activation and intensive chemical reaction did exist between TC, Cu₂O and PI (Fig. S33). In addition, with the increment of reaction temperature, the energy release was decreased and the reaction time shortened (Fig. S34), indicating that the reaction between Cu₂O and PI is an exothermic process. In contrast, the reaction rate could be improved by elevating reaction temperature due to the enhancement of Brownian motion [36]. Fitting the thermodynamic data reveals that the activation of PI by Cu₂O follows a pseudo-first-order kinetics (Fig. S35 and Table S3), which has not been revealed by other reports. These energy-releasing tests verified that the Cu₂O sample with {100}+{111}—2 co-exposed facets and {100}/{111} crystal edge is greatly active for PI activation compared to the ones with {100}/{110} and {110}/{111} crystal edges.

DFT calculation was further employed to investigate PI adsorption, the electron transfer and PI activation on Cu₂O surface with different facets/crystal edges (Fig. 4). The {100}/{111} crystal edge presented the lowest adsorption energy of −7.04 eV for PI activation among all the different types of facet edges, implied that the {100}/{111} crystal edges are profound for PI adsorption compared with other crystal edges and exposed facets. The corresponding charge density difference models after adsorption is illustrated in Fig. 4b, suggesting that the electrons are preferentially transferred from Cu₂O to PI in all models, which is conducive to the PI activation. Bader charge transfer from {100}/{111} crystal edge (0.95 e) exhibited the highest values among all models,

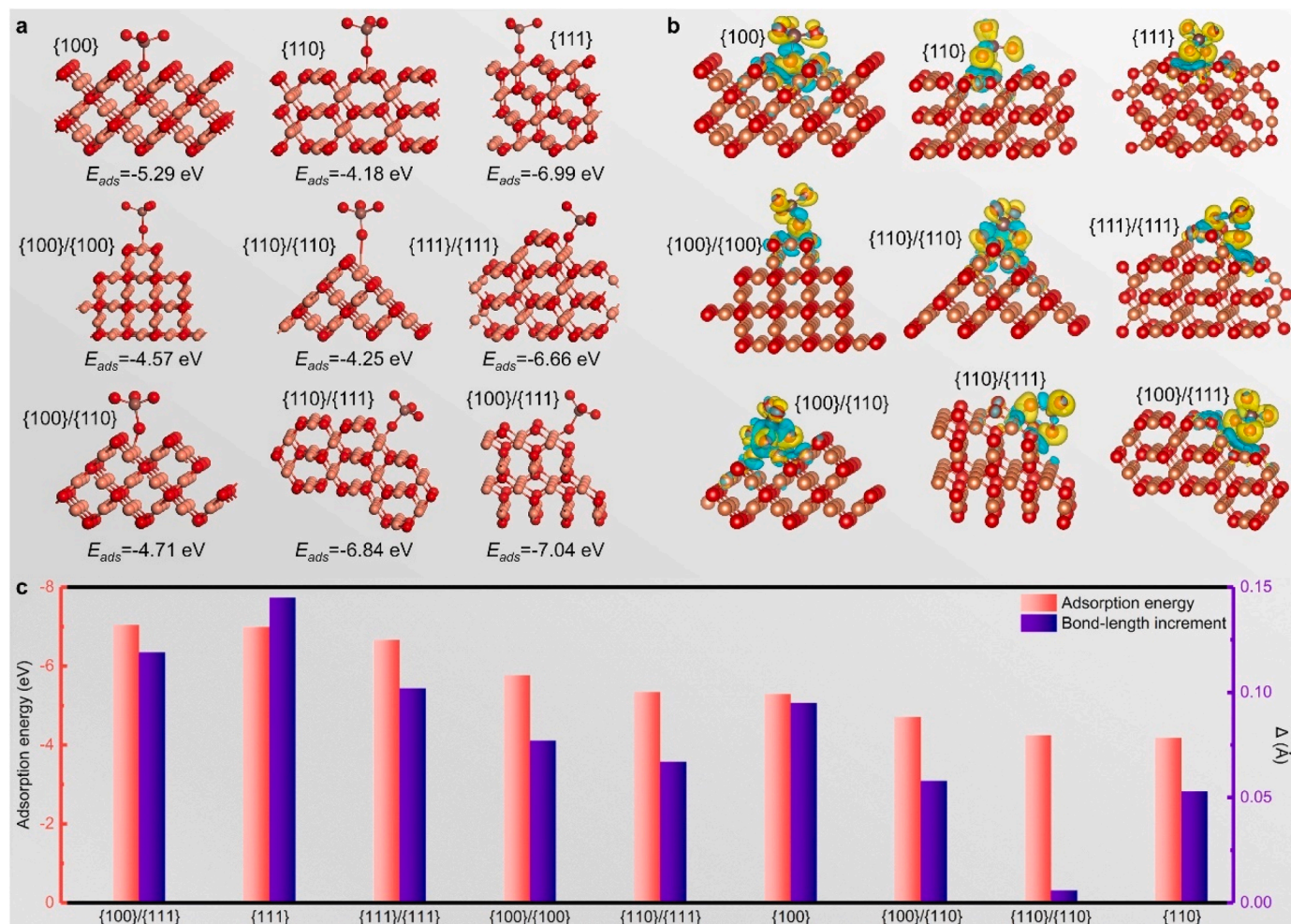


Fig. 4. DFT calculation of Cu₂O samples for PI activation. (a) Adsorption configurations of facets and crystal edges in Cu₂O towards PI activation. (b) Charge density difference of the corresponding adsorption models (yellow color indicates electron accumulation and green color means electron depletion). (c) Adsorption energies and I–O bond distance increment during Cu₂O activation PI process.

while the {100}/{110} and {110}/{111} crystal edges presented moderate Bader charge values compared with other relevant models. Meanwhile, the bond length of I–O in PI has been elongated from the original value of 1.861–1.980 Å (Fig. 4c) after adsorbed on {100}/{111} crystal edge, and the increment of 0.12 Å is more significant than most of the counterparts. The above analyses confirmed that the PI adsorbed on the {100}/{111} crystal edge are easier to be activated [37,38].

3.4. Practical evaluation

The influence of reaction parameters (catalyst dosage, PI concentration, pH, and coexisting anions) on TC degradation are investigated to regulate practical applications. Fig. 5a shows that TC degradation efficiency improves as the Cu₂O dosage increases from 0.05 g/L to 0.15 g/L. However, when the Cu₂O dosage was further increased to 0.20 g/L, a ~20% decrease in TC degradation efficiency was observed. The reason for the above phenomenon can be explained by the excess Cu ions brought by the higher Cu₂O dosage that scavenge the active species generated in the solution. In contrast, TC degradation efficiency increased with the increase of PI dosage due to that more active species were produced (Fig. 5b). The degradation efficiency of TC decreased from 97.57% (pH=3) to 77.37% (pH=10) as the rise of solution pH (Fig. 5c). The precipitation of copper hydroxide grows as the pH rises and adheres to Cu₂O surface to form an inert layer, thus hindering the PI activation [25]. Besides, the rising pH causes the dominant form of PI to be converted from IO₄⁻ to H₃IO₆²⁻, and the lower reduction potential of the latter (IO₄⁻/IO₃⁻ = 1.298 V, H₃IO₆²⁻/IO₃⁻ = 0.686 V) enlarges the electrostatic repulsion between Cu₂O surface and PI, and reduces the PI activation efficiency [37]. Moreover, Fig. 5d, e suggest that TC degradation is less affected by coexisting anions and water matrices due to the high selectivity of ¹O₂.

As a crucial factor for practical applications of catalysts, the cyclic catalytic performance of seven Cu₂O samples was also carried out (Figs. S36 and S37). It can be found that the four samples with {110}, {111}, {100}+{111}-1 and {100}+{111}-2 exposed facets

exhibited a relatively poor catalytic stability and about 25% catalytic rate was reduced after 5 cycles, while other three samples with {100}, {100}+{110} and {100}+{110}+{111} exposed facets displayed relatively good catalytic stability and only about 8% catalytic rate was declined after 5 cycles. The reasons could be ascribed to the adsorption of the degradation intermediate, Cu⁺/Cu²⁺ ratio in crystal and the corrosion of crystal, etc. The detailed discussion has been documented within supporting information (Figs. S38–S42, Tables S4 and S5).

Moreover, the catalytic activity of {100}+{111}-2 has also been compared with those of commonly-used catalysts, e.g. CuO, Fe₂O₃, Co₃O₄, Fe₃O₄, FeS₂, and also commercial Cu₂O (Fig. 5f, S43 and S44) [38–42]. Intriguingly, the sample Cu₂O with {100}+{111}-2 exposed facet shows about 6-fold higher *k*_{obs} than other composite materials, and ca. 4 and 2.5-fold higher *k*_{obs} than the reported ones CuO and commercial Cu₂O, respectively. Besides, the catalytic activity of Cu₂O with {100}+{111}co-exposed facets outperforms most reported works (Table S6), indicating that crystal edges regulation and facet engineering are equally important in the treatment of organic wastewater by AOPs.

Since the pollutants may be decomposed into some more toxic intermediates, it is necessary to evaluate the toxicity during TC degradation. Therefore, the intermediates of TC degraded by the 100 + 111-2/PI/SSL system were detected by LC-MS. As shown in Fig. S45, seven major intermediates with *m/z* = 475, 416, 383, 366, 252, 222, and 114 were detected. Therefore, three pathways for TC degradation were proposed (Fig. 6a). In pathway I, TC was converted to TC1 (*m/z* = 416) due to demethylation [4]. In pathway II, TC was firstly converted to TC2 (*m/z* = 383) via hydroxylation, demethylation, amination, benzene ring oxidation and hydroxyl oxidation. Then, TC3 (*m/z* = 297) was formed through ring opening, hydroxyl oxidation and decarbonylation of TC2 due to the attack of ·OH and ¹O₂ [1]. Subsequently, TC3 was oxidized to TC9 (*m/z* = 114) through a series of deamidation, ring opening, decarbonylation and carbonyl reduction due to the further oxidation of ¹O₂ [5]. In pathway III, the double bond in TC was oxidized firstly, followed by hydroxylation and dehydrogenation to form TC4 (*m/z* = 475). TC5 (*m/z* = 450) was formed after TC4 underwent

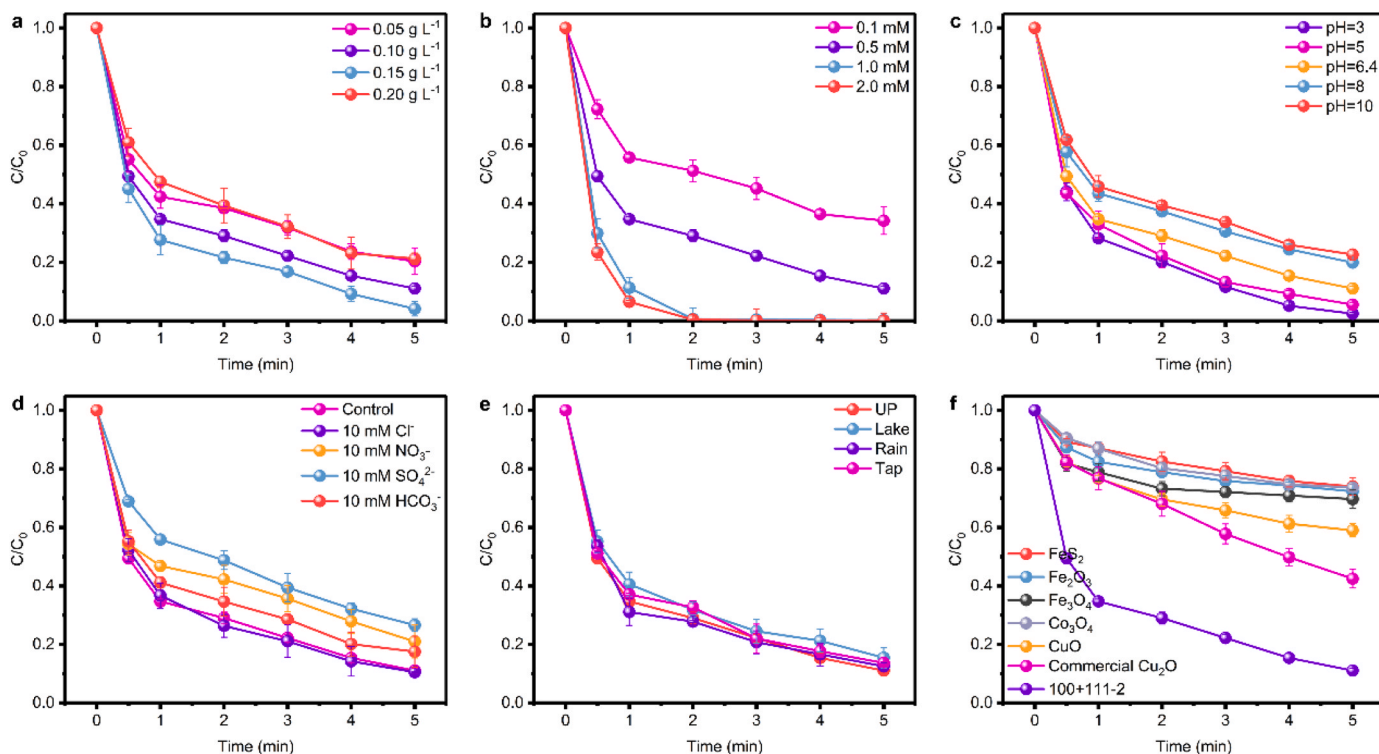


Fig. 5. Effect of (a) Cu₂O dosage, (b) PI dosage, (c) pH, (d) anions, and (e) different water matrixes on TC degradation. (f) Comparison of the activity of different catalysts for TC degradation. ([TC]₀ = 20 mg L⁻¹, with simulated sunlight).

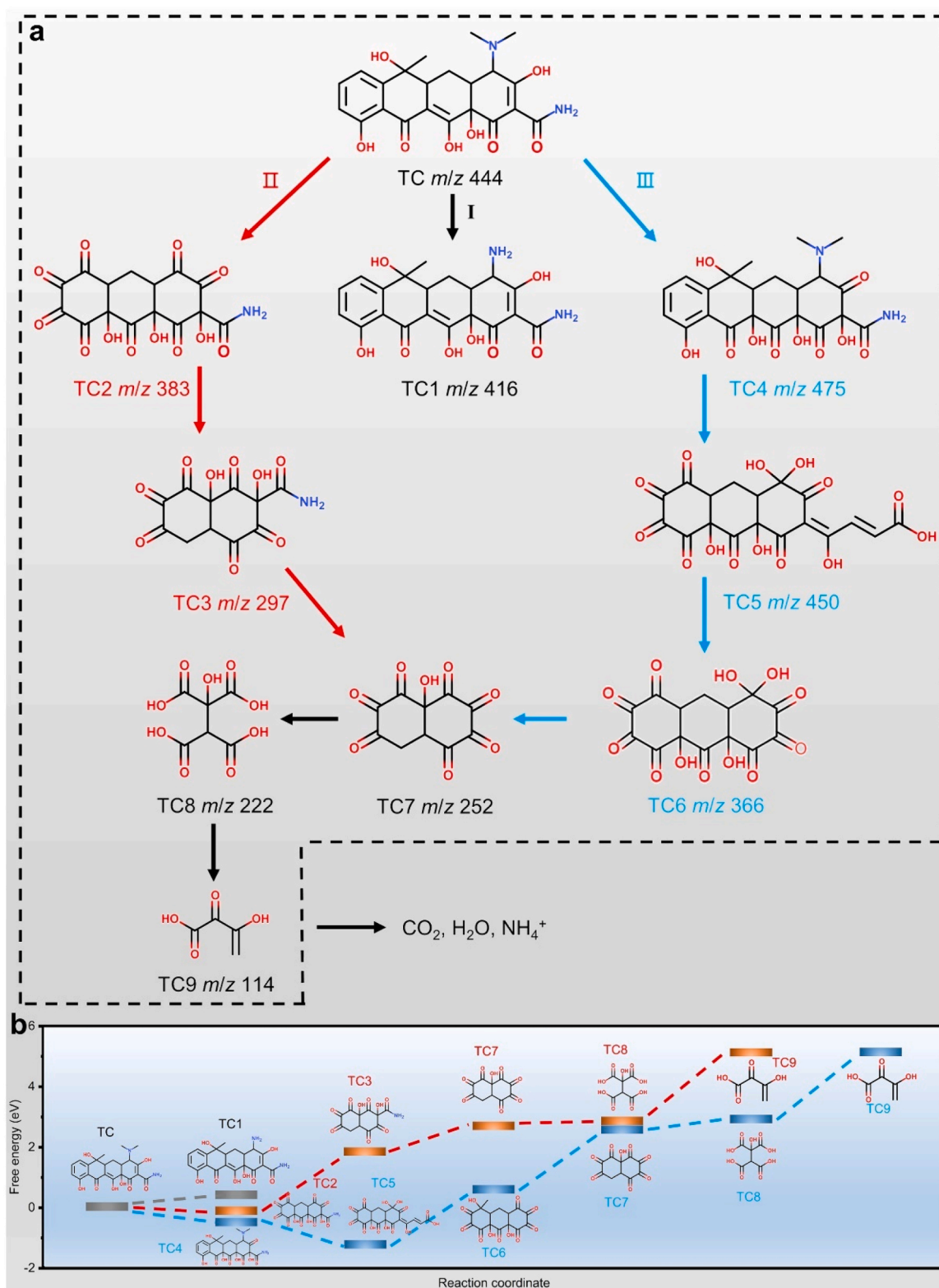


Fig. 6. (a) Proposed TC degradation pathways. (b) Calculated Gibbs free energy for three possible TC degradation pathways.

ring-opening, demethylation, deamination, hydrolysis reaction, double-bond hydroxylation and oxidation [2]. Due to the ¹O₂ attack, TC5 was then decomposed to TC6 ($m/z = 366$) via double-bond cleavage and carbonylation. After ring opening, TC6 was carbonylated to TC7 and further decomposed to TC9. Moreover, it is explicit that the pathway III is more energetically favorable than the other two pathways (Fig. 6b).

Then, the toxicity of TC and intermediates is assessed by the ECOSAR 2.2 program and the results are shown in Fig. 7a. Among the preliminary degradation products of TC, the median lethal dose (LC₅₀) and chronic toxicity (ChV) of TC1 and TC2 are decreased, while the toxicity of TC4 is increased compared with TC molecules. However, with the advancement of the degradation process, the toxicity of TC1, TC8,

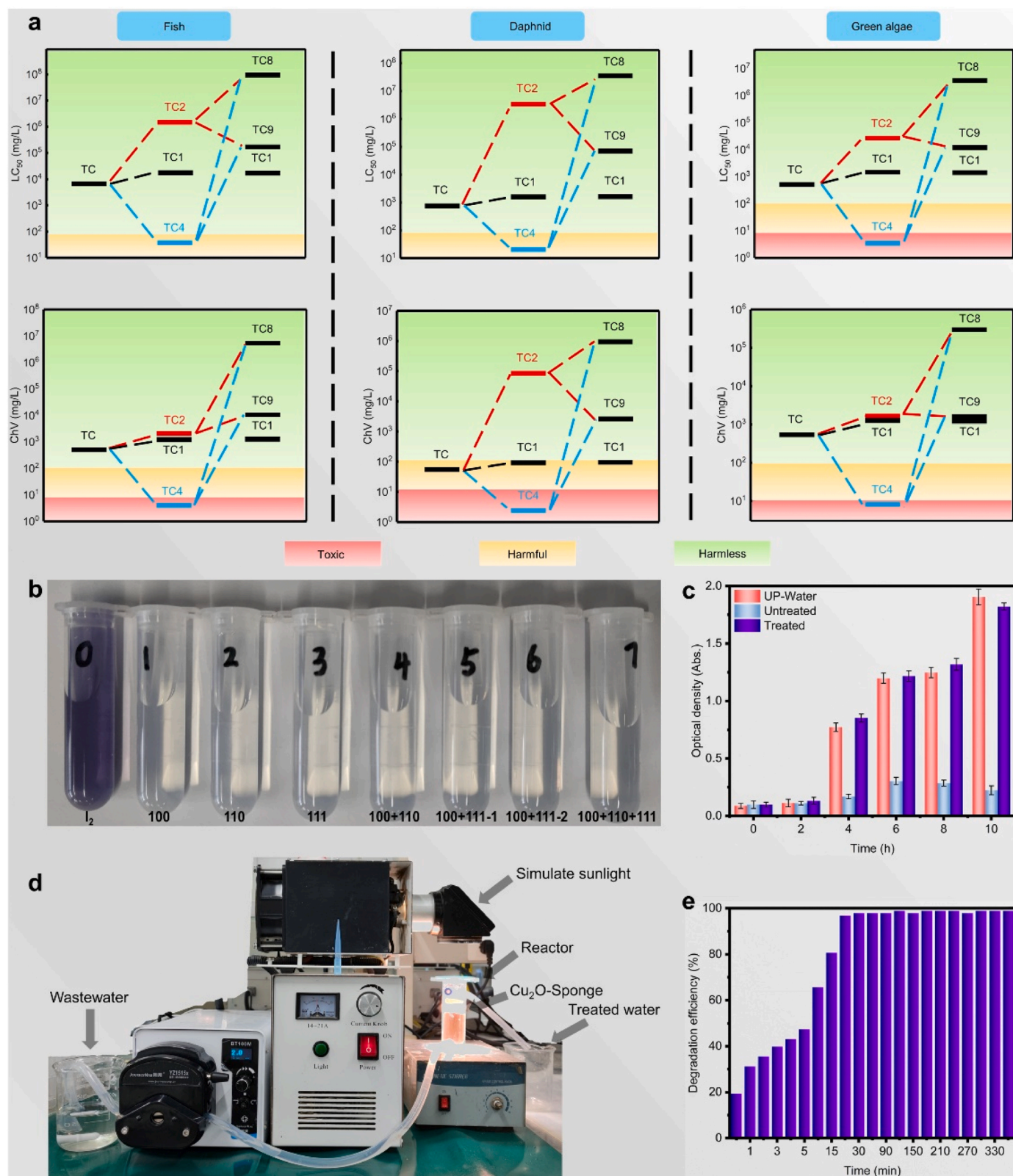


Fig. 7. (a) Toxicity assessment of TC and degradation intermediates. (b) Toxic I_2 and I_3 identification in PI decomposition products. (c) Growth curves of *E. coli* K12 in different culture medias. (d) Continuous flow treatment device. (e) Continuous flow treatment efficiency. ($[TC]_0 = 5 \text{ mg L}^{-1}$, $[catalyst]_0 = 0.1 \text{ g/L}$, $[PI]_0 = 0.5 \text{ mM}$, $Q_{input} = 6.2 \text{ mL min}^{-1}$, with simulated sunlight).

and TC9, which may exist at the terminal, is significantly reduced compared with TC molecules. In addition, the treated TC wastewater is colorless after reacting with the starch indicator, while I_2 shows a clear blue color (Fig. 7b). The above phenomenon demonstrates that toxic I_2 and I_3 are not generated in the $Cu_2O/PI/SSL$ system. Moreover, the toxicity of treated TC wastewater is similar to ultrapure water and did not inhibit the growth of *E. coli* (Fig. 7c). The above toxicity assessment indicates that the degradation of TC in the $100 + 111-2/PI/SSL$ system is do a decontamination process.

Besides, from the viewpoint of practical application, the continuous flow TC degradation treatment is also tested. As depicted in Fig. S45 and Table S7, Cu_2O with $\{100\} + \{111\} - 2$ facets is uniformly loaded onto the sponge after a simple impregnation treatment. More importantly, Cu_2O -Sponge is used for TC degradation in a flowing state (Fig. 7d), which could reach 100% within 20 min and maintain an excellent removal efficiency for at least 6 h (Fig. 7e), indicating the great potential of Cu_2O after facets regulation as a catalyst for practical wastewater treatment.

4. Conclusions

A series of single crystalline Cu_2O nanocrystals with different preferred facets exposure, together with the substantial crystal edge structures, have been successfully prepared to systematically study the effect of crystal edges formed among multi-exposed facets on the PI activation towards TC degradation under solar light. Intriguingly, Cu_2O with $\{100\} + \{111\}$ exposed facets and $\{100\}/\{111\}$ crystal edges presented the best TC degradation capability, being superior over those of $\{100\} + \{110\}$, $\{100\} + \{110\} + \{111\}$ multi-exposed ones with various crystal edges and $\{100\}$, $\{110\}$ as well as $\{111\}$ solely exposed ones, also over lots of well-documented PI activation catalysts and the commercial Cu_2O . The outstanding performance should be assigned to the superior properties of $\{100\}/\{111\}$ crystal edge. Various measurements and DFT calculations unraveled that the $\{100\}/\{111\}$ crystal edge with special atomic arrangement feature is beneficial for PI adsorption, electron transfer, and PI activation, finally leading to superior TC degradation performance. This work provides systematical insights into the critical crystal edge effects of single crystalline nanocrystals for high-efficiency catalytic performance, which paves the way for developing highly efficient catalysts for wastewater treatment via crystal edge engineering.

CRedit authorship contribution statement

Y.L. and X.W. conceived the idea, and designed the experiments. J. W. synthesized the materials and conducted various tests. W.L. and W.D. carried out the in-situ microcalorimetry test. Z.W. dedicated to the DFT calculations. Q.Z. estimated the electrochemical test. Q.M. conducted the SEM. X.F., H. C. performed the TEM measurement and structural analysis. Y.L. wrote the manuscript. X.W., H.C. revised the manuscript. All authors are dedicated to the discussion and revision of the manuscript.

Declaration of Competing Interest

The authors declare that they have no known competing financial interests or personal relationships that could have appeared to influence the work reported in this paper.

Data Availability

Data will be made available on request.

Acknowledgements

This work was supported by the National Key Research and

Development Program of China (No. 2021YFA1202500), National Natural Science Foundation of China (Nos. 21975193 and 51602237), and the Fundamental Research Funds for the Central Universities, China (WUT: 2021III034JC).

Appendix A. Supporting information

Supplementary data associated with this article can be found in the online version at doi:10.1016/j.apcatb.2023.123351.

References

- [1] C. Du, S. He, Y. Xing, Q. Zhao, C. Yu, X. Su, J. Feng, J. Sun, S. Dong, Fabricating S-scheme BiOBr/Zn₂In₂S₅ heterojunction for synergistic adsorption-photocatalytic degradation of tetracycline, Mater. Today Phys. 27 (2022), 100827.
- [2] H. Ren, F. Qi, A. Labidi, J. Zhao, H. Wang, Y. Xin, J. Luo, C. Wang, hemically bonded carbon quantum dots/Bi₂WO₆ S-scheme heterojunction for boosted photocatalytic antibiotic degradation: interfacial engineering and mechanism insight, Appl. Catal. B: Environ. 330 (2023), 122587.
- [3] M. Xu, J. Deng, A. Cai, X. Ma, J. Li, Q. Li, X. Li, Comparison of UVC and UVC/persulfate processes for tetracycline removal in water, Chem. Eng. J. 384 (2020), 123320.
- [4] N. Barhoumi, H. Olvera-Vargas, N. Oturan, D. Huguenot, A. Gadri, S. Ammar, E. Brillas, M. Oturan, Kinetics of oxidative degradation/mineralization pathways of the antibiotic tetracycline by the novel heterogeneous electro-Fenton process with solid catalyst chalcocopyrite, Appl. Catal. B: Environ. 384 (2017) 637–647.
- [5] J. Du, J. Bao, Y. Liu, H. Ling, H. Zheng, S. Kim, D. Dionysiou, Efficient activation of peroxymonosulfate by magnetic Mn-MGO for degradation of bisphenol A, J. Hazard. Mater. 320 (2016) 150–159.
- [6] P. Yang, X. Zhang, F. Gao, Y. Zheng, Z. Niu, X. Yu, R. Liu, Z. Wu, S. Qin, L. Chi, Y. Duan, T. Ma, X. Zheng, J. Zhu, H. Wang, M. Gao, S. Yu, Protecting copper oxidation state via intermediate confinement for selective CO₂ electroreduction to C₂₊ fuels, J. Am. Chem. Soc. 142 (2020) 6400–6408.
- [7] G. Liu, F. Zheng, J. Li, G. Zeng, Y. Ye, D. Larson, J. Yano, E. Crumlin, J. Ager, L. Wang, F. Toma, Investigation and mitigation of degradation mechanisms in Cu₂O photoelectrodes for CO₂ reduction to ethylene, Nat. Energy 6 (2021) 1124–1132.
- [8] S. Zhang, Y. Zhao, R. Shi, C. Zhou, G. Waterhouse, Z. Wang, Y. Weng, T. Zhang, Sub-3 nm ultrafine Cu₂O for visible light driven nitrogen fixation, Angew. Chem. Int. Ed. 60 (2021) 2554–2560.
- [9] S. Deng, V. Tjoa, H. Fan, H. Tan, D. Sayle, M. Olivo, S. Mhaisalkar, J. Wei, C. Sow, Reduced graphene oxide conjugated Cu₂O nanowire mesocrystals for high-performance NO₂ gas sensor, J. Am. Chem. Soc. 134 (2012) 4905–4917.
- [10] X. Zhou, Z. Liu, Y. Wang, Y. Ding, Facet effect of Co₃O₄ nanocrystals on visible-light driven water oxidation, Appl. Catal. B 237 (2018) 74–84.
- [11] R. Lin, J. Wan, Y. Xiong, K. Wu, W. Cheong, G. Zhou, D. Wang, Q. Peng, C. Chen, Y. Li, Quantitative study of charge carrier dynamics in well-defined WO₃ nanowires and nanosheets: insight into the crystal facet effect in photocatalysis, J. Am. Chem. Soc. 140 (2018) 9078–9082.
- [12] C. Wang, S. Jia, Y. Zhang, Y. Nian, Y. Wang, Y. Han, Y. Liu, H. Ren, S. Wu, K. Yao, X. Han, Catalytic reactivity of Co₃O₄ with different facets in the hydrogen abstraction of phenol by persulfate, Appl. Catal. B 270 (2020), 118819.
- [13] L. Hu, Q. Peng, Y. Li, Selective synthesis of Co₃O₄ nanocrystal with different shape and crystal plane effect on catalytic property for methane combustion, J. Am. Chem. Soc. 130 (2008) 16136–16137.
- [14] J. Meng, Y. Duan, S. Jing, J. Ma, K. Wang, K. Zhou, C. Ban, Y. Wang, B. Hu, D. Yu, L. Gan, X. Zhou, Facet junction of BiOBr nanosheets boosting spatial charge separation for CO₂ photoreduction, Nano Energy 92 (2022), 106671.
- [15] X. Cheng, X. Dao, S. Wang, J. Zhao, W. Sun, Enhanced Photocatalytic CO₂ reduction activity over NH₂-MIL-125(Ti) by facet regulation, ACS Catal. 11 (2021) 650–658.
- [16] J. Ke, J. Zhao, M. Chi, M. Wang, X. Kong, Q. Chang, W. Zhou, C. Long, J. Zeng, Z. Geng, Facet-dependent electrooxidation of propylene into propylene oxide over Ag₃PO₄ crystals, Nat. Commun. 13 (2022), 932.
- [17] S. Chen, L. Wang, Z. Li, Y. Xiong, Facet-engineered surface and interface design of monoclinic scheelite bismuth vanadate for enhanced photocatalytic performance, ACS Catal. 10 (2020) 1024–1059.
- [18] L. Mu, Y. Zhao, A. Li, S. Wang, Z. Wang, J. Yang, Y. Wang, T. Liu, R. Chen, J. Zhu, F. Fan, R. Li, C. Li, Enhancing charge separation on high symmetry SrTiO₃ exposed with anisotropic facets for photocatalytic water splitting, Energy Environ. Sci. 9 (2016) 2463–2469.
- [19] Q. Li, P. Xu, B. Zhang, H. Tsai, S. Zheng, G. Wu, H. Wang, Structure-dependent electrocatalytic properties of Cu₂O nanocrystals for oxygen reduction reaction, J. Phys. Chem. C. 117 (2013) 13872–13878.
- [20] L. Tang, J. Lv, Z. Yang, Facile hydroxyl-assisted synthesis of morphological Cu₂O architectures and their shape-dependent photocatalytic performances, N. J. Chem. 38 (2014) 4656–4660.
- [21] W. Huang, L. Lyu, Y. Yang, M. Huang, Synthesis of Cu₂O nanocrystals from cubic to rhombic dodecahedral structures and their comparative photocatalytic activity, J. Am. Chem. Soc. 134 (2012) 1261–1267.

- [22] H. Luo, B. Li, J. Ma, P. Cheng, Surface modification of nano-Cu₂O for controlling CO₂ electrochemical reduction to ethylene and syngas, *Angew. Chem. Int. Ed.* 61 (2022), e202116736.
- [23] Y. Shang, L. Guo, Facet-controlled synthetic strategy of Cu₂O-based crystals for catalysis and sensing, *Adv. Sci.* 2 (2015) 1500140.
- [24] J. Wang, J. Fan, J. Yao, X. Wu, C. Gao, Z. Wei, Y. Li, Facet tailoring and Cu doping promoted photo-assisted peroxymonosulfate activation by oxygen-deficient alpha-MnO₂ for efficient mineralization of bisphenol a, *Chem. Eng. J.* 461 (2023), 142024.
- [25] C. Ling, S. Wu, J. Han, T. Dong, C. Zhu, X. Li, L. Xu, Y. Zhang, M. Zhou, Y. Pan, Sulfide-modified zero-valent iron activated periodate for sulfadiazine removal: performance and dominant routine of reactive species production, *Water Res.* 220 (2022), 118676.
- [26] Y. Zong, Y. Shao, Y. Zeng, B. Shao, L. Xu, Z. Zhao, W. Liu, D. Wu, Enhanced oxidation of organic contaminants by iron(II)-activated periodate: the significance of high-valent iron-oxo species, *Environ. Sci. Technol.* 55 (2021) 7634–7642.
- [27] J. Du, G. Xiao, Y. Xi, X. Zhu, F. Su, S. Kim, Periodate activation with manganese oxides for sulfanilamide degradation, *Water Res.* 169 (2020), 115278.
- [28] Z. Guo, Y. Si, W. Xia, F. Wang, H. Liu, C. Yang, W. Zhang, W. Li, Electron delocalization triggers nonradical Fenton-like catalysis over spinel oxides, *Proc. Natl. Acad. Sci. USA* 119 (2022), e2201607119.
- [29] B. Kim, J. Kim, P. Tsai, H. Choi, S. Yoon, S. Lin, D. Kim, Large surface photovoltage of WS₂/MoS₂ and MoS₂/WS₂ vertical hetero-bilayers, *ACS Appl. Electron. Mater.* 3 (2021) 2601–2606.
- [30] Y. Jia, L. Zhang, L. Zhuang, H. Liu, X. Yan, X. Wang, J. Liu, J. Wang, Y. Zheng, Z. Xiao, Identification of active sites for acidic oxygen reduction on carbon catalysts with and without nitrogen doping, *Nat. Catal.* 2 (2019) 688–695.
- [31] J. Yang, J. Jing, W. Li, Y. Zhu, Electron donor–acceptor interface of TPPS/PDI boosting charge transfer for efficient photocatalytic hydrogen evolution, *Adv. Sci.* 9 (2022), 2201134.
- [32] P. Shao, Y. Jing, X. Duan, H. Lin, L. Yang, W. Ren, F. Deng, B. Li, X. Luo, S. Wang, Revisiting the graphitized nanodiamond-mediated activation of peroxymonosulfate: singlet oxygenation versus electron transfer, *Environ. Sci. Technol.* 55 (2021) 16078–16087.
- [33] Z. Wu, M. Karamad, X. Yong, Q. Huang, D. Cullen, P. Zhu, C. Xia, Q. Xiao, M. Shakouri, F. Chen, J. Kim, Y. Xia, K. Heck, Y. Hu, M. Wong, Q. Li, I. Gates, S. Siahrostami, H. Wang, Electrochemical ammonia synthesis via nitrate reduction on Fe single atom catalyst, *Nat. Commun.* 12 (2021), 2870.
- [34] F. Yao, M. Jia, Q. Yang, F. Chen, Y. Zhong, S. Chen, L. He, Z. Pi, K. Hou, D. Wang, Highly selective electrochemical nitrate reduction using copper phosphide self-supported copper foam electrode: performance, mechanism, and application, *Water Res.* 193 (2021), 116881.
- [35] S. Zheng, J. Hu, K. Chen, J. Yao, Z. Yu, X. Lin, Soil microbial activity measured by microcalorimetry in response to long-term fertilization regimes and available phosphorous on heat evolution, *Soil Biol. Biochem.* 41 (2009) 2094–2099.
- [36] L. Yang, Y. Xiang, F. Jia, L. Xia, C. Gao, X. Wu, L. Peng, J. Liu, S. Song, Photo-thermal synergy for boosting photo-Fenton activity with rGO-ZnFe₂O₄: novel photo-activation process and mechanism toward environment remediation, *Appl. Catal. B* 292 (2021), 120198.
- [37] L. He, C. Yang, J. Ding, M. Lu, C. Chen, G. Wang, J. Jiang, L. Ding, G. Liu, N. Ren, Fe, N-doped carbonaceous catalyst activating periodate for micropollutant removal: significant role of electron transfer, *Appl. Catal. B* 303 (2022), 120880.
- [38] W. Xu, W. Xue, H. Huang, J. Wang, C. Zhong, D. Mei, Morphology controlled synthesis of α -Fe₂O_{3-x} with benzimidazole-modified Fe-MOFs for enhanced photo-Fenton-like catalysis, *Appl. Catal. B* 291 (2021), 120129.
- [39] J. Lee, U. von Gunten, J. Kim, Persulfate-based advanced oxidation: critical assessment of opportunities and roadblocks, *Environ. Sci. Technol.* 54 (2020) 3064–3081.
- [40] W. Liu, Y. Wang, Z. Ai, L. Zhang, Hydrothermal synthesis of FeS₂ as a high-efficiency fenton reagent to degrade alachlor via superoxide-mediated Fe(II)/Fe(III) cycle, *ACS Appl. Mater. Interfaces* 7 (2015) 28534–28544.
- [41] W. Wang, Y. Liu, Y. Yue, H. Wang, G. Cheng, C. Gao, C. Chen, Y. Ai, Z. Chen, X. Wang, The confined interlayer growth of ultrathin two-dimensional Fe₃O₄ nanosheets with enriched oxygen vacancies for peroxymonosulfate activation, *ACS Catal.* 11 (2021) 11256–11265.
- [42] J. Wang, S. Wang, Activation of persulfate (PS) and peroxymonosulfate (PMS) and application for the degradation of emerging contaminants, *Chem. Eng. J.* 334 (2018) 1502–1517.